JOURNAL OF MATERIALS SCIENCE 22 (1987) 3361–3367

Investigation of laser irradiation of WC–Co cemented carbides inside a scanning electron microscope (LASEM)

B. SCHULTRICH, K. WETZIG
Akademie der Wissenschaften der DDR, Zentralinstitut für Festkörperphysik und Werkstofforschung, DDR-8027 Dresden, GDR

A combination of scanning electron microscope and laser enables direct observation of structural modifications by a high-energy input. With this new device melting phenomena and fracture processes in a WC–6% Co hard metal were investigated. The first laser pulse leads to melting of a thin surface layer with the formation of blisters and craters. Further pulses effect only small changes. This is attributed to exhaustion of the driving forces exerted from highly compressed pores. Cracking is induced by the relaxation of compressive surface stresses during the high-temperature stage and the appearance of tensile stresses during cooling. Besides crack formation and extension, complete welding of crack surfaces was observed after repeated laser irradiation.

1. Introduction

Short-time high-power input as irradiation by a laser or electron beam is an effective means for modifying surfaces or for studying thermal damage [1, 2]. Furthermore, high-temperature states are frozen in by self-quenching and thus become accessible to subsequent investigation at room temperature. The information gained by such experiments would be greatly increased if the structural changes (usually in the submicroscopic range) could be followed by comparing the same place before and after irradiation. This is possible by means of a novel arrangement combining the high power concentration of a laser with the high resolution of a scanning electron microscope (LASEM). A short description of the first LASEM equipment is given in Section 2. In the following this new arrangement is used for investigation of high-temperature effects in WC–Co cemented carbides. This fine-grained material (mean size of carbide grains $\approx 1\,\mu m$) realizes the interesting case of the combination of a high-melting material (T_m (WC) $\approx$ 2700° C) with some amount of a second phase with lower melting point (T_m (Co (W, C)) $\approx$ 1300° C, volume fraction $f \approx 10$ to 40%).

2. Equipment for laser irradiation in the SEM (LASEM)

In order to enable an effective investigation of laser–material interactions a scanning electron microscope (Jeol JSM S1) was combined with a pulsed laser [3–5]. The neodymium–glass laser employed yields in the free generation mode an energy per pulse of about 3 J at pulse lengths of some milliseconds.

Under the focusing conditions used (spot area $\approx$ 0.1 mm^2) this corresponds to an average power density of about 10^6 W cm^{-2}. By means of a Q switch, the pulse time can be diminished to some 10^{-8} sec and thus the power density is increased up to 10^{10} W cm^{-2}, taking into account the reduction of beam energy by a factor of ten. Lately, a similar equipment has been described by Chapliev *et al.* [6]. They use a microsecond-pulsed CO_2 laser with a repetition frequency of 200 Hz and an output energy of 0.5 J.

The combination of laser and SEM column is schematically shown in Fig. 1. On the top of the neodymium–glass laser and along its optical axis an He–Ne laser is situated for optical adjustment of the laser beam. The radiation of both lasers is deflected into the SEM by an adjustable mirror and focused on the specimen by an optical system. The position of the laser spot, marked by the visible radiation of the He–Ne laser, can be controlled by a window opposite the laser beam entrance. Some mechanical and electrical adaptations of the SEM were necessary for protecting SEM functions against laser-induced optical and electrical perturbations. Thus, a flexible aperture protection and a sector screen for detector protection were constructed. The electrical components with the power supply for the laser include an electrical safety device to protect the SEM electronics from damage.

The usual operation mode consists in imaging the selected surface region before and after the first and subsequent laser pulses. During irradiation microscopic observation is not possible because of the necessary shielding of the detector. The input angle of the laser beam (related to the surface normal) can be varied between 50 and 70°. Both top face and side face can be observed.

3. Surface melting of WC–Co

The structural and topographic changes on the surfaces of WC–Co cemented carbides by high-power input have been comprehensively discussed [7] for the case of a Q-switched neodymium–glass laser. The

0022–2461/87 $03.00 + .12

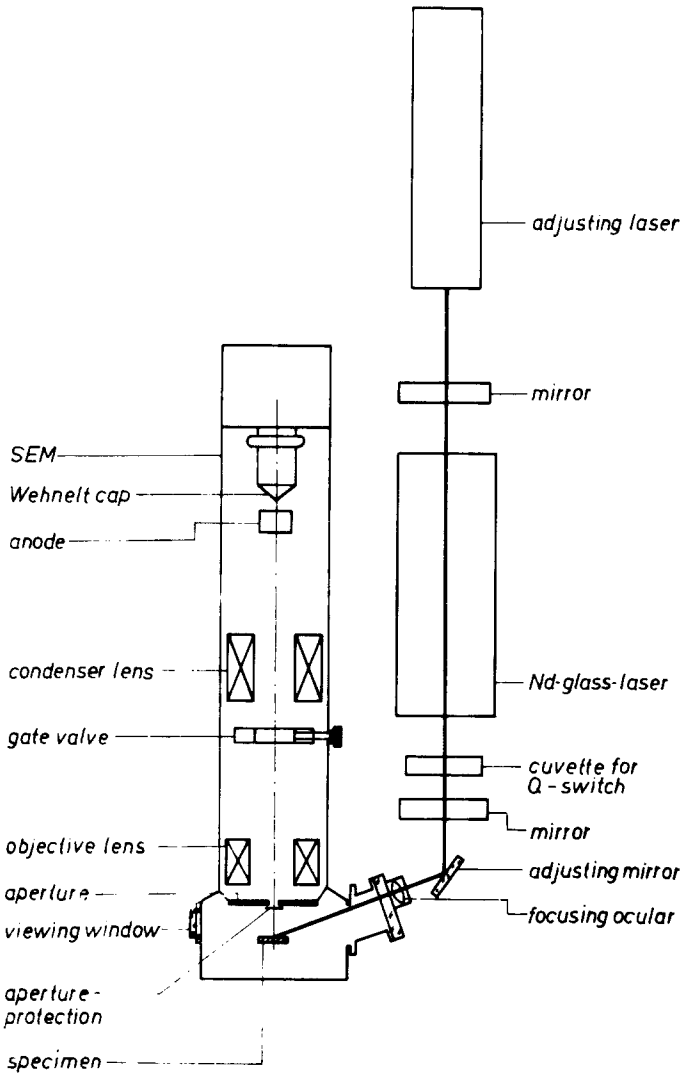

Figure 1 Scheme of the combination of laser and scanning electron microscope (LASEM).

main results can be summarized as follows:

1. Besides the hexagonal α-WC and fcc Co the high-temperature phase of cubic β-WC_z (z = 0.6 to 1), stable above 2500° C, occurs.
2. A thin surface layer of about 1 μm is melted. Its grain size lies well below the original one.
3. The melted surface layer is inflated by expanding gases included in micropores, thus roughening the surface (mean roughness 1 to 2 μm). Sometimes these blisters burst, leaving small holes or larger craters.
4. That fraction of the incident laser energy which is absorbed within the target is nearly independent of surface roughness. Nevertheless, visible melting effects according to items 2 and 3 above appear much more pronounced on samples with ground surface than on polished ones.

The investigations with the LASEM equipment confirm these statements. By observing the same surface region in successive irradiation stages, they also reveal new and unexpected features of the laser-induced surface modifications. Fig. 2 shows the changing appearance of a ground WC–6% Co hard metal from the as-received state (Fig. 2a) to that after one (Fig. 2b) and three (Fig. 2c) laser pulses (Q-switch mode) for a region near the boundary of the irradiation spot. In this zone the underlying grinding structure is partially conserved after the first and subsequent laser pulses in regions with a smaller energy input (right-hand side in Figs 2b and c) as can be seen from the grinding marks. The irregular distribution of molten areas in this region may be attributed to inhomogeneities in laser beam energy as well as an inhomogeneous distribution of pores near the surface. On open pores acting as absorbing cavities, better coupling conditions may cause local melting. Closed pores just below the surface develop the driving force for dislocating the molten layer, thus producing visible topographical changes. In regions with a higher energy input (left-hand side in Figs 2b and c) the original structure has completely disappeared and has been replaced by the usual wavy melt layer with hollow blisters and microholes. As a rule microholes are lying on top of the blisters, thus indicating the formation of roughness by bursting blisters. Surprisingly, the subsequent laser pulses barely change this structure; it seems to be invariant against repeated melting (Fig. 2c). Some blisters expand further and burst (circled region), thus revealing their hollowness. Furthermore some additional micropores appear. For successive laser pulses the energy input and hence the surface temperature and viscosity should be nearly the same. However, it seems that the driving force for changing the surface topography, namely the supply of gas expanding and erupting from the melt layer, is exhausted.

The experiment was repeated with polished surfaces of the same material, with the result shown in Fig. 3.

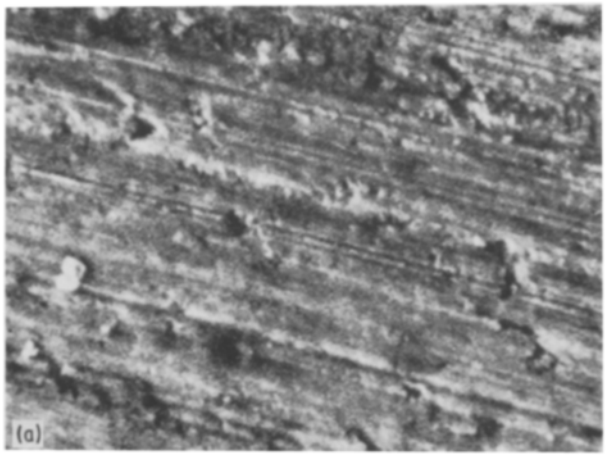

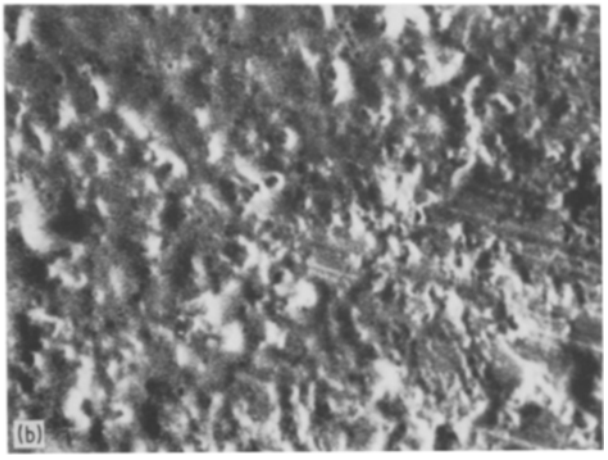

Figure 2 Surface of a ground WC–6% Co hardmetal irradiated with a *Q*-switched neodymium–glass laser: (a) as-received state, (b) after first laser pulse (boundary region), (c) after third laser pulse (boundary region).

In the SEM micrographs the angular WC grains appear bright, the cobalt binder phase grey and pores or holes black. Again the figures represent the structural modifications near the spot boundary (Fig. 3b). (The laser spot is marked by the grey region encircled with dashed lines.) But only small topographical changes are induced by laser irradiation in this case, notwithstanding the comparable energy input. No melting of the carbide phase appears in the pictured boundary zone. As a most remarkable phenomenon, small (mostly shallow) grooves appear (Fig. 3b). Thorough comparison with the initial state (Fig. 3a) shows that they are left behind from evaporated binder regions. Further laser pulses on the same spot yield no visible change in the boundary region. Therefore the seventh pulse was centred on the observed region (Fig. 3c). Melting then revealed itself by blistering and bursting. The shallow grooves from binder evaporation are levelled off in this region. The deeper holes (occurring in Fig. 3b as black holes) are conserved or expand, suggesting their role as open channels (circled regions). The craters are not correlated with former binder regions.

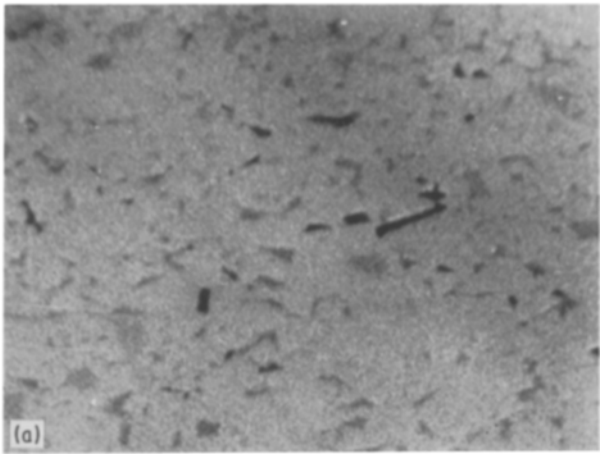

Figure 3 Surface of a polished WC–6% Co hardmetal irradiated with a *Q*-switched neodymium–glass laser: (a) as-received state, (b) after first laser pulse (boundary region), (c) after seventh laser pulse displaced such that the observed region lies in the spot centre.

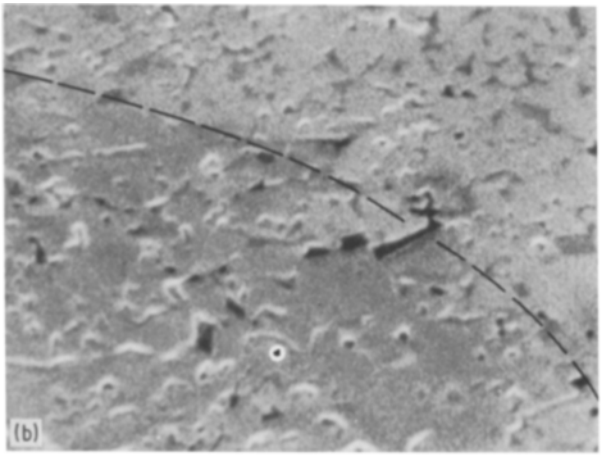

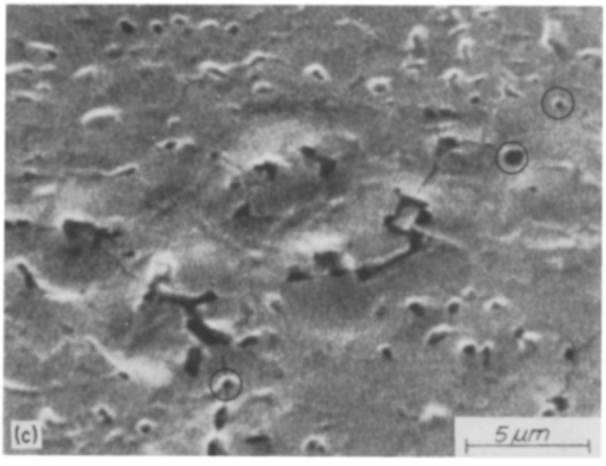

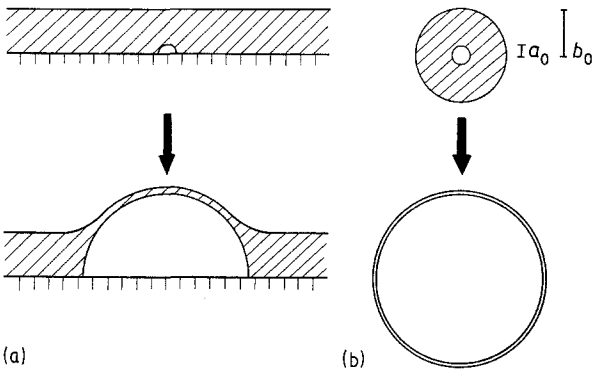

Figure 4 Bubble model of laser-induced roughening: (a) blistering of the melt layer, (b) modelling by a viscous hollow sphere.

A quantitative estimate of blister formation in the viscous molten layer gives some insight into the driving forces of this process. For a rough approximation it is modelled by the isothermal expansion of a viscous hollow sphere with enclosed and compressed ideal gas (Fig. 4). A rise of circumferential stress due to wall thinning over-compensates the decrease of pressure. Hence, the outer bubble radius b will exponentially increase (see Appendix):

$$b(t) = b_0 \, e^{t/t^*} \quad \text{with} \quad t^* = 4\eta v/p_0 \quad (1)$$

Here, η denotes viscosity and v the ratio of shell to pore volume at the beginning, which is related to the initial outer and inner radii b_0 and a_0 by $v = (b_0/a_0)^3 - 1$. From this, the initial internal pressure p_0, the driving force for bubble expansion, can be calculated as

$$p_0 = \frac{4\eta v}{\Delta t \ln (b_f/b_0)} \quad (2)$$

with final radius b_f of the sphere resolidified after time Δt. The inner radius a_0 corresponds to the enclosed pores for which $a_0 \approx 0.2\,\mu m$ is assumed. The initial outer radius b_0 is given by the thickness of the molten layer ($\approx 1\,\mu m$) and its final value b_f may be estimated by the laser-induced roughness ($b_f \approx 2$ to $3\,\mu m$), giving a value of nearly unity for the weakly varying logarithm. Using twice the pulse time, 5×10^{-8} sec, for the time Δt in the molten viscous state (during heating and cooling) and viscosity $\eta = 0.1$ Pa sec (as given for oxide melts 100 K above the melting point), from Equation 2 a high value $p_0 \approx 1000$ MPa for the necessary driving pressure follows. Even in the limiting case of a superheated melt with water-like fluidity ($\eta \approx 0.001$ Pa sec) a remarkable pressure of $p_0 \approx 10$ MPa must be exceeded.

These pressures may now be compared with the effects of potential sources of expanding gases. In the case of partial melting, the temperature in the molten layer will be stabilized not too far from the melting point of tungsten carbides at 2700° C. The boiling point of cobalt lies at 3200° C. Hence, the pressure of evaporating cobalt vapour of about 0.1 MPa (= 1 atm) is much smaller than the estimated bubble pressure. The gas in the pores may be entrapped by closing the initial open ones at normal pressure (0.1 MPa) during densification by liquid-phase sintering (at about 1400° C). By laser heating the gas pressure will rise in proportion with the absolute temperatures to $p_0 = 0.1\,\text{MPa} \times 3000\,\text{K}/1700\,\text{K} \approx 0.2\,\text{MPa}$. Again this lies well below the necessary value. It is however well known that the grinding of hard metals induces high internal compressive stresses of about 500 to 1000 MPa in the surface, up to a depth of 10 to 30 μm (see e.g. [8]), indicating intense plastic deformation. It is anticipated that the pores will be strongly compressed during this process, the increasing internal pressure being inversely proportional to the volume ratio. For instance, compression from a pore radius of 1 μm to 0.2 μm corresponds to a rise in pressure by a factor of about 100. Together with the factor from the temperature ratio mentioned above, this yields pressures $p_0 \approx 200$ MPa. Contrary to the other mechanisms discussed, they are of the right order.

Accepting this compressed pore mechanism for laser blistering in WC–Co cemented carbides, surface melting is not necessarily connected with surface roughening. By polishing, the heavily deformed grinding layer is removed without inducing new deformations, as is verified by the vanishing of internal stresses (apart from phase stresses from material heterogeneity and anisotropy) [8]. Now that the near-surface pores are in the uncompressed state, the main driving force for displacing the melt is lacking, and recrystallization reproduces the original structure.

Additional small effects may be contributed by capillary forces. Surface tension ($\gamma = 1\,\text{N m}^{-1}$) yields at curvatures of $r \approx 0.1\,\mu m$ stresses of the order of $\gamma/r \approx 10$ MPa, leading to some rounding of sharp corners and droplike phenomena [7].

4. Thermal cracking

The sudden rise of the surface temperature to values far above that of the surrounding substrate and its subsequent rapid cooling by self-quenching can cause the formation and propagation of cracks. Such cracks result from the superposition of inhomogeneous thermal expansion and stress relaxation by creep [9, 10]. Thermal expansion of the heated surface is suppressed by the cold surroundings, resulting in compressive stresses parallel to the surface. They are relaxed by high-temperature creep which allows the material to move in the unrestricted direction, normal to surface plane. However, in subsequent cooling tension is caused by thermal contraction which may result in crack networks. Their depths and spacings depend on the power density and pulse time [7].

Under the irradiation conditions used for the investigations of Section 3, thermal cracking is observed only in the spot centre. Fig. 5 shows this region for the laser spot of Fig. 2 on a ground WC–6% Co hard metal. Its development demonstrates similar features as in the boundary zone (Fig. 2), but in a more pronounced manner. Blisters and their central craters (mostly existing here) are larger, corresponding to the higher temperatures and lower viscosity of the melt in this region. Nevertheless, after these marked changes by the first laser pulse the subsequent ones cause only minor further modifications. Some new cracks arise (arrows) and crack opening increases in general, improving their visibility. As a rule, cracks cross the

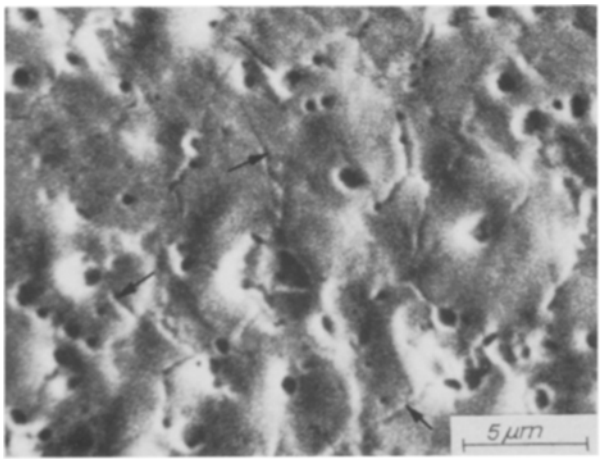

Figure 5 Centre region of same spot as in Fig. 2 after eighth laser pulse.

burst blisters and traverse microholes or craters, indicating strength degradation of the surface layer which has delaminated from the compact there. Laser-induced crack formation on polished samples is shown in Fig. 6 for the same experimental conditions as in Fig. 3. Again the marginal region of the laser spot shows neither melting nor cracks except for the broken-up bubble shown, probably produced by a larger pore just below the surface (Fig. 6a). Some new cracks or extended ones are the only remarkable changes after successive identically placed laser pulses. In order to increase the incident energy density, the spot centre was displaced towards the observed regions before the seventh pulse. Besides levelling off structural features (marked by evaporated binder), bubbling and cratering, the formation and extension of cracks is now much intensified (Fig. 6b). But also for these stronger irradiation conditions repeated laser pulses lead to insignificant topographical changes, and only some new or extended cracks.

As is usual in dense crack networks due to stress shielding, the depth of the cracks corresponds to their mutual distance (see e.g. [11]). For the laser-induced cracks discussed above, it may be estimated to be 10 μm. This marks the highly stressed region, where cracks are produced already from small defects on the grain level of 1 μm and below. The relaxed zone itself is much more extended, but in general the stresses are too small for further crack propagation. They are sufficient for cracking from macroscopic defects, as they are created near a fracture surface (Fig. 7a). The relaxed region which contracts during the localized cooling acts as an inclusion with a larger thermal expansion coefficient which undergoes homogeneous cooling. The largest tensile stresses arise at and normal to the boundary. Considering the free surface, cracking starts at the outer points, where stresses are directed parallel to surface (Fig. 7b). From there the contracting region is partly peeled out.

In general cracks are produced by laser treatment, but sometimes they are removed by some kind of welding process. The visible crack traces may be masked by superficial filling or overlaying with molten material [7]. Apart from these trivial cases, surprisingly, crack healing far below the molten layer is also possible. This unusual behaviour is demonstrated in Fig. 8. It shows observations from the side of a ground WC–6% Co hard metal after unswitched irradiation.

Again, better visibility is attained by producing large laser-induced cracks from preformed defects on the fracture surface. After the first pulse the typical blister and crater surface has been formed with a large crack (Fig. 8a). Further pulses leave the topography unchanged, as seen from craters on the irradiated top side and crystallites just below. However, the crack has completely closed over the whole length shown of more than 50 μm, without any traces left (Fig. 8b). A new crack was produced instead about 10 μm to the right (besides an independent smaller one on the right). The difference between the two cracks is revealed best by looking for surface marks which lie on the right side of the crack in its first stage but on the left in the second one (circled regions). This welding may be explained by local sintering under the high compressive stresses during the laser pulse. At a larger depth this is incomplete due to lower pressures and temperatures. From there the remaining crack breaks through to the surface along a new path, when tension builds up during cooling.

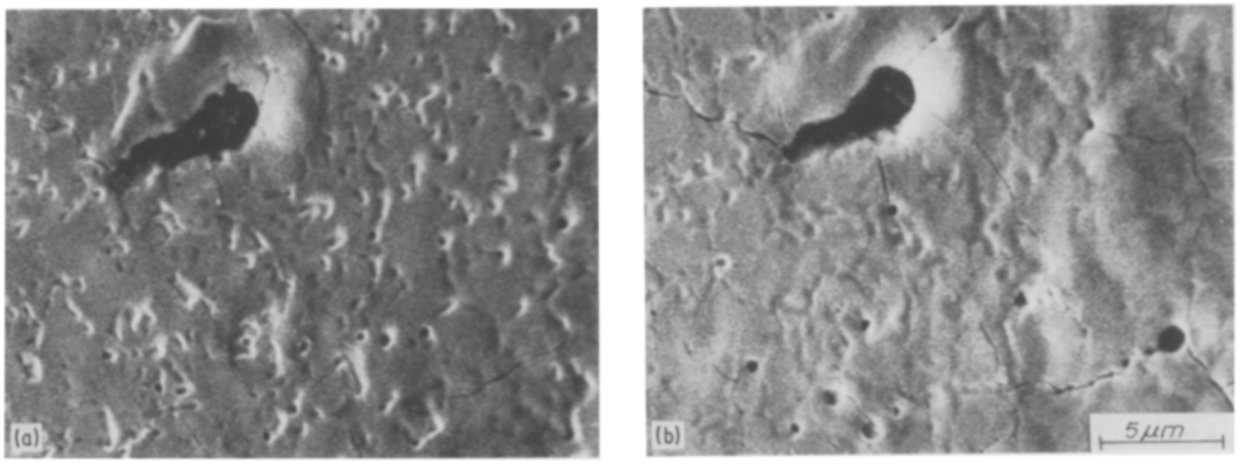

Figure 6 Surface of a polished WC–6% Co hardmetal irradiated (as in Fig. 3) with a *Q*-switched neodymium–glass laser. (a) After second laser pulse (boundary region); note higher energy input and local melting around large pore. (b) After twelfth laser pulse; local energy input was increased by displacing the spot centre towards the region of investigation.

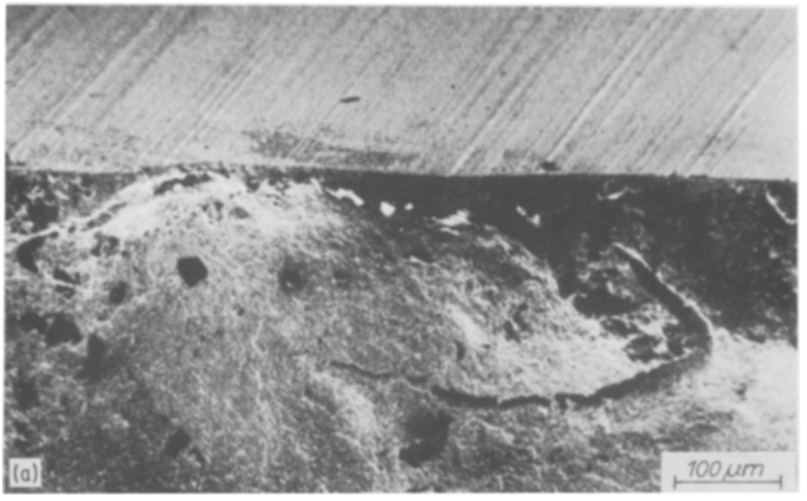

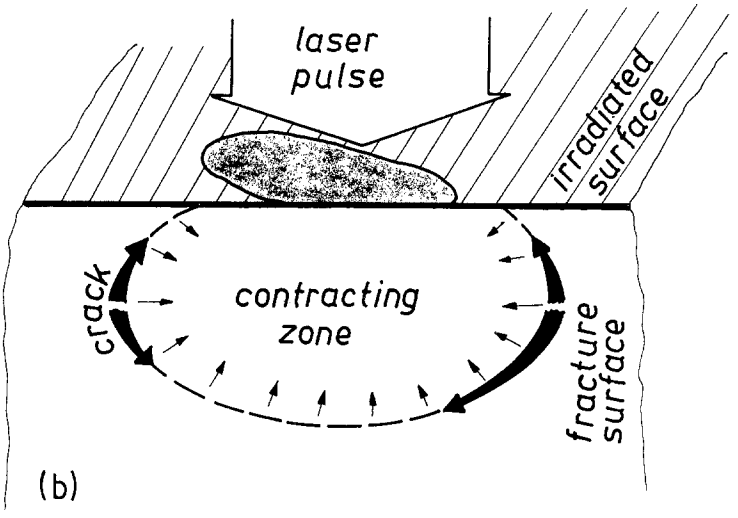

Figure 7 (a) Side view of fracture surface (bottom) with macroscopic cracks induced by Q-switched laser pulses on the ground surface (top) of a WC–6% Co hardmetal. The spot was situated near the fracture centre (at the origin of the radial fracture marks). (b) Scheme of macroscopic crack propagation along the relaxation zone boundary.

Acknowledgements

The authors would like to thank Dr H. J. Scheibe for assistance in the installation of LASEM, Dr J. Edelmann for experimental help and Dr H. J. Weiss for critical discussion.

Appendix

For problems with spherical symmetry the velocity field $\boldsymbol{v}(\boldsymbol{r}, t)$ is given by $\boldsymbol{v}(\boldsymbol{r}, t) = v(r, t)\ \boldsymbol{r}/r$ and the deformation velocity β by $\beta_{rr} = \mathrm{d}v/\mathrm{d}r$ and $\beta_{\theta\theta} = \beta_{\phi\phi} \equiv \beta_{tt} = v/r$. From the assumed incompressibility of the viscous material with $\beta_{rr} + 2\beta_{tt} = 0$ the general solution $v(r, t) = f(t)/r^2$ follows. The viscous material equation $\sigma_{ik} = 2\eta\beta_{ik} - q\delta_{ik}$ couples stresses δ_{ik} and deformation velocities β_{ik}. (q denotes a function $q(r, t)$ which follows from incompressibility.) The

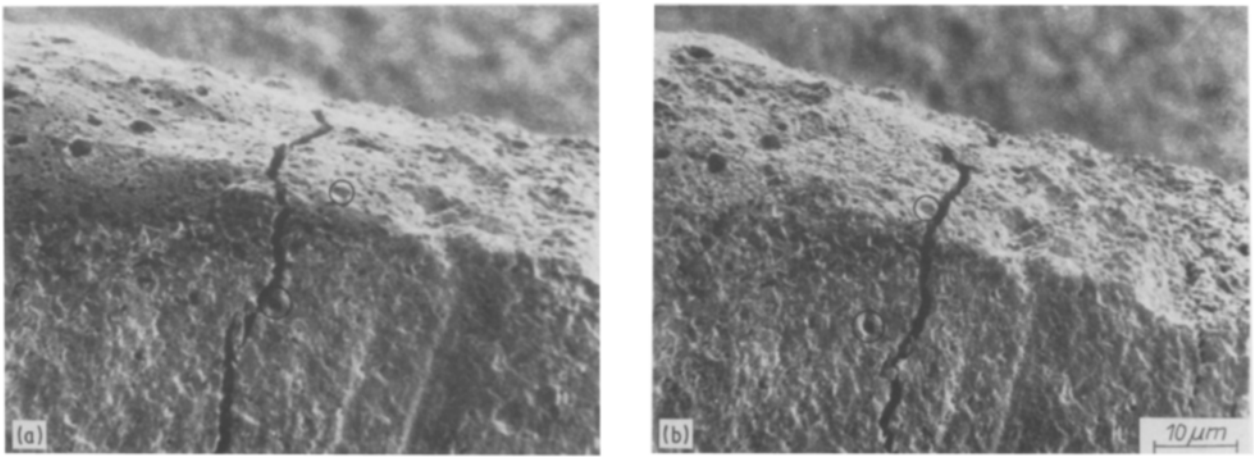

Figure 8 Side view of ground surface (bottom) with macroscopic cracks induced by unswitched laser pulses on the fracture surface of a WC–6% Co hardmetal. (a) After first laser pulse. (b) After third laser pulse; original crack has closed but opened again along a new path (see marked structural details).

equilibrium condition

$$\frac{\partial \sigma_{rr}}{\partial r} + \frac{2}{r}(\sigma_{rr} + \sigma_{tt}) = -\frac{\partial q}{\partial r}$$

is identically fulfilled by $q(r, t) = q(t)$.

The expansion of a hollow viscous sphere with inner pressure p (Fig. 4) is described by the boundary conditions $\sigma_{rr} = 0$ at the outer surface $r = b$ and $\sigma_{rr} = -p(t)$ at $r = a$. Both radii are connected by volume conservation: $b(t)^3 - a(t)^3 = b_0^3 - a_0^3$, where zero subscripts denote the initial state. This yields

$$\frac{p(t)}{4\eta} \frac{a^3 b^3}{b_0^3 - a_0^3} = f(t) = r^2 \frac{\mathrm{d}r}{\mathrm{d}t} = \frac{1}{3} \frac{\mathrm{d}b^3}{\mathrm{d}t}$$

For isothermal expansion of an enclosed ideal gas pV = constant or $p(t)a(t)^3 = p_0 a_0^3$. With this we get the differential equation

$$\frac{\mathrm{d}b^3}{\mathrm{d}t} = \frac{3}{4\eta} \frac{p_0 a_0^3}{b_0^3 - a_0^3} b^3$$

with the solution

$$b^3 = b_0^3 \exp\left(\frac{3}{4\eta} \frac{p_0 a_0^3}{b_0^3 - a_0^3} t\right)$$

or $b(t)$ as used in Equation 1.

References

1. J. MAZUMDER, *J. Metals* **35**(5) (1983) 18.
2. B. ROEBUCK and E. G. BENNETT, in Proceedings of 11th Plansee Seminar, Reutte, May 1985.
3. K. WETZIG, J. EDELMANN, W. FISCHER, W. POMPE, H. J. SCHEIBE, B. SCHULTRICH and W. RESCH, Wirtschaftspatent DD 238 207 (1985).
4. J. EDELMANN, H. J. SCHEIBE, K. WETZIG, K. LENZ, B. SCHULTRICH, W. POMPE and W. FISCHER, in Proceedings of 5th International Conference on Laser Applications, Dresden, 1985.
5. K. WETZIG, J. EDELMANN and H. J. SCHEIBE, in Proceedings of 11th International Congress on Electron Microscopy, Kyoto, 1986, Vol. 1, p. 333.
6. N. I. CHAPLIEV, V. I. KONOV, S. M. PIMENOV and A. M. PROCHOROV, in Proceedings of 2nd International Conference on Trends in Quantum Electronics, Bucharest, 1985, p. 197.
7. B. SCHULTRICH, H. J. SCHEIBE, M. ERMRICH and W. POMPE, to be published.
8. B. O. JAENSSON, *Mater. Sci. Engng.* **8** (1971) 41.
9. A. SOLINA, M. de SANCTIS, L. PAGANINI, A. BLARASIN and S. QUARANTA, *J. Heat Treating* **3** (1984) 193.
10. M. R. JAMES, D. S. GNANAMUTHU and R. J. MOORES, *Scripta Metall.* **18** (1984) 357.
11. G. GILLE, *Curr. Topics Mater. Sci.* **12** (1985) 421.

Received 4 November 1986
and accepted 28 January 1987